

ADDING SENSITIVITY TO 21CM INTERFEROMETRIC PROBES OF REIONIZATION BY OPTIMIZING CHOICE OF BASELINES

YUNFAN GERRY ZHANG¹, AARON R. PARSONS^{1,2}

¹Astronomy Dept., U. California, Berkeley, CA

²Radio Astronomy Lab., U. California, Berkeley, CA

ABSTRACT

We introduce an accurate method to extract additional sensitivity from data of redundant radio arrays. Our method efficiently finds optimal baselines to cross correlate, including baselines that are slightly different in length and orientation. Using the latest and final 128-element version of Precision Array for Probing the Epoch of Reionization (PAPER-128), as well as the planned 37, 128, 240 and 350 element versions of the Hydrogen Epoch of Reionization Array (HERA) now under development, we illustrate how our method applies to different array configurations and predict the sensitivity improvements of including each baseline pairs. The extremely natural and simple implementation of this method would increase the sensitivity of PAPER-128 by up to [50] percent, and increase the out-rigger imaging sensitivity of HERA-350 by a factor of 2.

1. INTRODUCTION

The epoch of reionization, or cosmic dawn represents the last key stage of the universe’s early evolution. Study of this event stands at the intersection of cosmology and astrophysics. Understanding this event is important not only because it is a scientific goal of its own, but also because it can provide crucial information to fundamental nature of inflation, neutrino mass and phenomenology of the first stars and galaxies (e.g. ?).

Arguably the most promising observational probe of the epoch of reionization comes from measurement of the “spin-flip” transition of neutral hydrogen of characteristic wavelength 21cm ???. While probes such as quasar spectra rely on emission and scattering of free electrons, and are thus limited to the lower redshifts after the completion of reionization, the 21cm line directly probes the abundance and distribution of neutral hydrogen, and thus would potentially shed light on all stages of reionization. Radio interferometry efforts to measure the 21cm power spectrum has been a top priority in recent years of astronomy. Current generation instruments include the Precision Array for Probing the Epoch of Reionization (PAPER) ??, Murchison Wide-field Array (MWA) ?, Low Frequency Array (LOFAR) ?, and next generation instruments such as the Hydrogen Epoch of Reionization Array (HERA) (e.g. ????), and the Square Kilometer Array Low (SKA low) (e.g. ?) are under construction.

One of the main challenges of interferometric observations of cosmic 21cm line is the foreground contamination. Both sources within our galaxy, and to a lesser distant sources outside of our galaxy emit radio contaminations (via for example synchrotron processes) up to five orders of magnitude stronger than the reioniza-

tion signal. There are two common methods to deal with the foreground contamination. In the first, sometimes called the foreground removal technique, individual sources are identified and removed in the image domain. The other technique, commonly referred to as ‘foreground avoidance’, makes use of the fact that most common foreground contaminations have a smooth spectrum, and thus is constrained to a Fourier domain “foreground wedge” ??. Thus contamination can be avoided by restricting our observation to “outside the wedge”, where the data is currently noise dominated. The main challenge of using the avoidance technique is thus the sensitivity, or the signal to noise ratio. This is the motivation for the design of the maximum redundancy arrays such as PAPER and HERA. While traditional imaging arrays focus on Fourier mode uv coverage, the redundant arrays focus on redundant measurements of the same Fourier mode with many tightly packed antennas at equal spacing. Since baselines of the same length and orientation measure the same Fourier modes on the sky, a maximum redundancy array is able to increase the signal to noise ratio by averaging over measurements of the same baseline. ? provides the newest upper limit to the power spectrum measurements with the PAPER-64 data. From some models we roughly expect that the sensitivity required for detection is a factor of 10 away. This paper explores a new technique to add sensitivity to the analysis of redundant arrays, by making use of the earth’s rotation. This technique can be applied to redundant arrays such as PAPER and HERA to increase the sensitivity by up to a factor of [1.5].

The earth’s rotation causes the baselines to pick up different modes of the sky with time. This effect is used extensively to improve uv coverage in imaging with minimum redundancy arrays. In a maximally redundant ar-

ray, baselines that are slightly different rotate into each other at a time delay. Here we present a method to improve the sensitivity of the maximum redundancy arrays by including the uv redundancy of different baselines at a time lag. It's worth noting as recent progress the authors of ? proposes an algorithmic search approach to extract information from near-equivalent baselines. We here propose a simple and elegant theoretical formalism that in addition allows us to identify baselines to cross-correlate and predict the weight of sensitivity.

Baselines of the same length and orientation are traditionally called “redundant baselines”, because they measure the same Fourier mode in the sky. In order to eliminate confusion and ambiguity, we shall introduce slightly different terminology. We'll call baselines that are the same length and orientation “equivalent baselines”, inspired by the mathematical notion of equivalence classes. Two equivalent baselines will be redundant with each other simultaneously at all times. Non-equivalent baselines can also be partially redundant if their respected time series is shifted with respect to one another by a certain delay. In other words, one baseline can be “rotated into” another. We call these “near-equivalent baselines”. It is our goal to a) identify the near-equivalent baselines that give good redundancy, b) to find the optimal time offset for a given pair of baselines, and c) to quantify the sensitivity improvement associated with cross multiplying such a pair of near-equivalent baselines. In section 2 we explain the theoretical basis for this cross multiplication. In section 3 we present details of the numerical implementation of this technique. In section 4 we discuss the expected sensitivity improvement with this method for HERA and PAPER-128 and with section 5 we conclude.

2. METHOD

2.1. Rough Idea

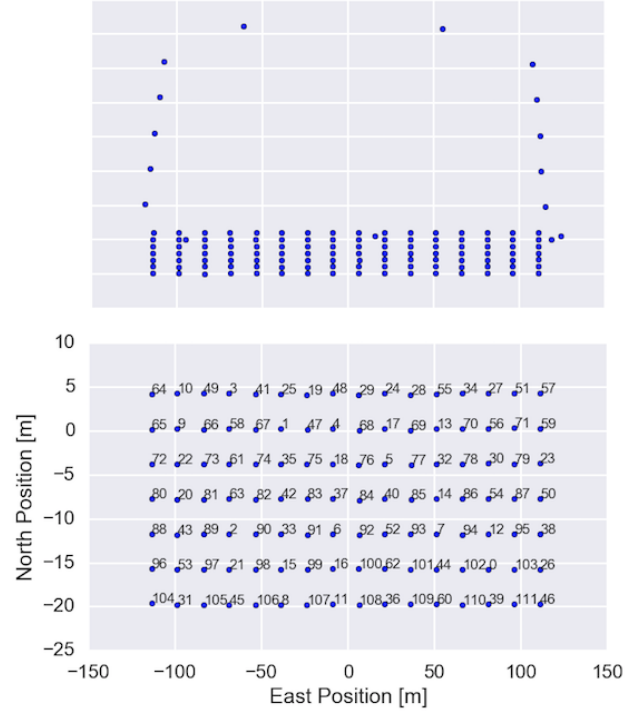


Figure 1. The PAPER-128 layout. Each blue dot corresponds to the location of an antenna. Top panel shows the antenna positions drawn to scale, bottom panel show the antenna labels and distances, excluding the outlier antennas. The numbering of the antennas the bottom panel are original labels during instrument assembly and does not bear significant meaning. Baselines corresponding to the same separations are called equivalent. In the bottom panel, the two baselines labeled with the red arrow are equivalent, with separation denoted by sep1,0, for the antennas are separated by 1 unit east and 0 unit north. Similarly, the baselines labeled with the yellow and green arrows are examples of sep1,1 and sep-1,1, respectively. Note sep1,0 and sep-1,0 for example are the same baselines and should not be counted twice.

We shall use the 128-element PAPER array to demonstrate. The PAPER array is located in the Karoo desert in South Africa (30:43:17.5 S, 21:25:41.8 E). The layout pattern with antenna labels are show in Fig. 1. We see the antenna spacing in North-South directions are comparatively close (4m), so that baselines such as 0_44 and 0_7 are very close to equivalent. In the bottom panel, the two baselines labeled with the red arrow are equivalent, with separation denoted by sep1,0, for the antennas are separated by 1 unit east and 0 unit north. Similarly, the baselines labeled with the yellow and green arrows are examples of sep1,1 and sep-1,1, respectively. Note sep1,0 and sep-1,0 for example are the same baselines and should not be counted twice. Antennas in purely north-south baselines are close enough to induce cross talks, and hence are not suitable for use. The original PAPER-64 analysis used three classes of baselines, here equivalent to sep2,0, sep2,1 and sep-2,1 ? of PAPER-128. There each of these classes of baselines are cross multiplied to itself. We shall see that in addition these baseline classes can be cross multiplied with a time off-

set.

Given a point source on the sky, each baseline maps the source to a point in uv plane. As the earth rotates with respect to the source, the point traces out tracks in the uv-plane. The uv tracks of PAPER-128 over 4.8 hours, at 0.15GHz, for a source that passes through zenith, are shown in Fig. 2.

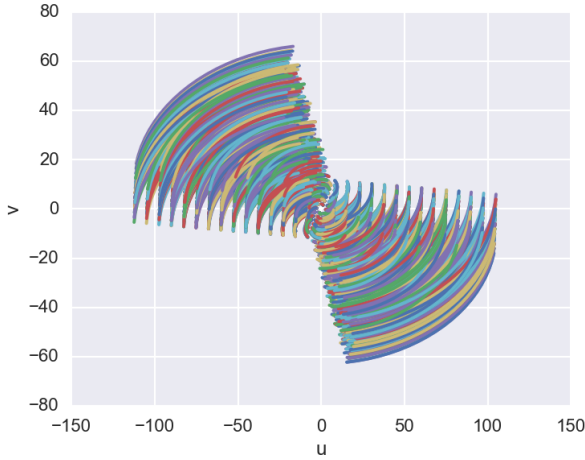


Figure 2. Tracks of PAPER-128 (grid only, excluding outliers) for a hypothetical source that passes through zenith. These tracks are traced out over 0.2 sidereal days, or roughly 4.8 hours. Color represents different baselines. Frequency is $\nu = 0.15\text{GHz}$. As the earth rotates, tracks are traced out counterclockwise.

Roughly speaking, we can identify redundancy of near-equivalent baselines as crossings of the uv tracks. Although this is a valid quick method to identify some baselines to cross-multiply, we find that it is not accurate enough for time offset determination. The reason is, for wide beam antennas such as PAPER, the sources are not point-like. In other words, when tracks of one point of the sky are crossing in uv-plane, those corresponding to another is not. To accurately constrain redundancy we must take into account of finite beam width. A more rigorous treatment is thus required. We show sample beams of HERA and PAPER antennas in Fig. 3 for reference.

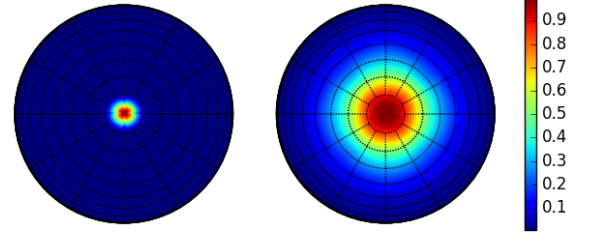


Figure 3. Sample beam response of HERA (left) and PAPER (right) antennas, both for frequency of $\nu = 150\text{MHz}$ and Stokes I polarization. Notice A in this paper is a “baseline’s beam”, equivalent to squares of the antenna beams shown here. The circles centered around zenith (center of beam) here are spaced 10 degrees apart. The finite size of the beams limits the accuracy of the uv track-crossing as a method of redundancy search.

2.2. Formalism

Below we shall derive theoretical expectations of cross multiplications of two near-equivalent baselines. More precisely we shall relate the product of visibilities of two different baselines to the power spectrum.

We take the visibility as commonly defined in the literature (e.g. ?):

$$\begin{aligned} V_\nu(b) &= \int d\Omega A_\nu(\hat{s}) \phi(\nu) I_\nu(\hat{s}) \exp \left[-2\pi i \frac{\nu}{c} \mathbf{b} \cdot \hat{s} \right], \\ &\approx \frac{2k_B}{\lambda^2} \int d\Omega A_\nu(\hat{s}) \phi(\nu) T(\hat{s}) \exp \left[-2\pi i \frac{\nu}{c} \mathbf{b} \cdot \hat{s} \right], \end{aligned} \quad (1)$$

Here λ is a mean wavelength, \mathbf{b} is the baseline length, \hat{s} and Ω are a direction in the sky and its corresponding solid angle. A_ν is the (frequency dependent) beam, and I is the specific intensity, which has been related to T , the brightness temperature in the Rayleigh-Jeans limit. Note that A here is the baseline beam, i.e. product of two antenna beams, examples of which are shown in Fig. 3. $\phi(\nu)$ is the frequency band profile. For PAPER, for example, the bands studied are roughly a top-hat from 144MHz to 154 MHz.

We define the delay transformed visibility ?:

$$\begin{aligned} V(b, \tau) &= \int d\nu V_\nu(b) \phi(\nu) \exp[-2\pi i \nu \tau], \\ &= \frac{2k_B}{\lambda^2} \int d\Omega d\nu A(\hat{s}, \nu) \phi(\nu) T(\hat{s}, \nu) \exp \left[-2\pi i \nu \left(\frac{\mathbf{b} \cdot \hat{s}}{c} + \tau \right) \right]. \end{aligned} \quad (2)$$

Eq. (2) expresses the delay-transformed visibility as an integral over observation coordinates \hat{s} and ν . Ulti-

mately, we would like to relate the data, collected with coordinates \hat{s} and ν , to the power spectrum, written with cosmological coordinates \mathbf{r} and \mathbf{k} . We start by noticing that [Gerry: change all \mathbf{r} and \mathbf{k} into bold]

$$\begin{aligned} r &= \frac{c}{H_0} \int_0^z \frac{dz'}{E(z')}, \\ &\approx \frac{c}{H_0} \int_0^{z_0} \frac{dz'}{E(z')} - \frac{c(1+z)^2}{\nu_{21} H_0 E(z)} (\nu - \nu_0), \\ &\equiv D_c - Y \Delta \nu, \end{aligned} \quad (3)$$

where $\nu_{21} = 1420 \text{ MHz}$ is the 21cm transition rest frequency, ν_0 a reference central frequency with corresponding redshift z_0 , and

$$E(z) = \sqrt{\Omega_m(1+z)^3 + \Omega_\Lambda}. \quad (4)$$

Inverting for ν :

$$\nu = \frac{D_c - r}{Y} + \nu_{21}. \quad (5)$$

Thus $d\nu = -dr/Y$ and $d^3r = -X^2 Y d\Omega d\nu$.

We can thus rewrite the delayed transformed visibility as

$$V(b, \tau) = \frac{1}{X^2 Y} \int_H d^3r A(\vec{r}) \phi(r) I(\vec{r}) \exp \left[-2\pi i \left(\frac{b}{c} \cdot \hat{r} + \tau \right) \nu_r \right]. \quad (6)$$

Here $(r_x, r_y, r_z) = (X\hat{s}_x, X\hat{s}_y, Y\nu)$, and $(Xk_x, Xk_y, Yk_z) = \frac{2\pi}{c}(b_x, b_y, \eta)$ relate the cosmological coordinates r and \mathbf{k} to the measured coordinates. We have written ν_r to remind us that ν and r are related by Eq. (5). The beam reception pattern A is dimensionless, normalized to 1 at its peak (zenith), and we assume it to be the same for all baselines.

With a time offset, the beam pattern has moved relative to the sky. Here we choose to fix the sky, and denote the rotated coordinates of the beam pattern with the operator Γ . With implicit bounds of integrals from $-\infty$ to ∞ , we have:

$$\begin{aligned} &\langle V^*(b, \tau) V(b', \tau') \rangle \\ &= \left(\frac{2k_B}{X^2 Y \lambda^2} \right)^2 \int d^3r d^3r' \langle T^*(r) T(r') \rangle A^*(r) A(\Gamma r') \Phi_{b, \tau}(r, \Gamma r'), \\ &= \left(\frac{2k_B}{X^2 Y \lambda^2} \right)^2 \int d^3r d^3r' \left(\int \frac{d^3\kappa}{(2\pi)^3} \frac{d^3\kappa'}{(2\pi)^3} \langle T^*(\kappa) T(\kappa') \rangle e^{-i(\kappa r - \kappa' r')} \right) A^*(r) A(\Gamma r') \Phi_{b, \tau}(r, \Gamma r'), \\ &= \left(\frac{2k_B}{X^2 Y \lambda^2} \right)^2 \int d^3r d^3r' \left(\int \frac{d^3\kappa}{(2\pi)^3} P(\kappa) e^{-i\kappa(r-r')} \right) A^*(r) A(\Gamma r') \Phi_{b, \tau}(r, \Gamma r'), \\ &= \left(\frac{2k_B}{X^2 Y \lambda^2} \right)^2 \int d^3r d^3r' \xi(r - r') A^*(r) A(\Gamma r') \Phi_{b, \tau}(r, \Gamma r'), \\ &\approx \left(\frac{2k_B}{X^2 Y \lambda^2} \right)^2 P(k_{b, \tau}) \int d^3r d^3r' \delta_D^{(3)}(r - r') A^*(r) A(\Gamma r') \Phi_{b, \tau}(r, \Gamma r'), \\ &= \left(\frac{2k_B}{X^2 Y \lambda^2} \right)^2 P(k_{b, \tau}) \int d^3r |A^*(r) A(\Gamma r)| |\phi(\nu_r)|^2 \exp \left[-i2\pi \nu_r \left(\hat{r} \cdot \frac{b}{c} - \hat{\Gamma r} \cdot \frac{b'}{c} \right) \right], \\ &= \left(\frac{2k_B}{\lambda^2} \right)^2 P(k_{b, \tau}) \int \frac{d\Omega d\nu}{X^2 Y} |A^*(\hat{s}, \nu) A(\hat{\Gamma s}, \nu)| |\phi(\nu)|^2 \exp \left[-i2\pi \nu \left(\hat{s} \cdot \frac{b}{c} - \hat{\Gamma s} \cdot \frac{b'}{c} \right) \right], \end{aligned} \quad (7)$$

where in transition from cosmological coordinates back to observing coordinates we have written $\hat{r} \equiv \hat{s}$, and

$$\Phi_{b, \tau}(r, \Gamma r') = |\phi^*(\nu_r) \phi(\nu_{r'})| \exp \left[-i \frac{2\pi}{c} \left(b \cdot \nu_r \hat{r} - b' \cdot \nu_{r'} \hat{\Gamma r'} \right) \right] \exp [-i2\pi \tau (\nu_r - \nu_{r'})]. \quad (8)$$

The second to third line of Eq.(7) follows from assumption of Gaussian random sky, and the third to fourth line follows from the assumption that the 3D power spectrum varies negligibly over the region of interest so that $\hat{P}_{21}(k+k_2) \approx P_{21}(k)$. Since Γ is a sky rotation, it doesn't affect ν , hence we have taken ν_r outside the parenthesis. Notice that the phase factor $\exp[-i2\pi\tau(\nu - \nu')]$ drops out in the end. This is significant because this means

that correlation is peaked at the same time-offset for all delay channels.

Finally, since the beam pattern and bandwidth are given in \hat{s} and ν , we convert the integral back to these coordinates to get the general relation between the delay-

transformed visibilities and the power spectrum:

$$\begin{aligned} & \langle V^*(b, \tau) V(b', \tau') \rangle \\ &= \left(\frac{2k_B}{\lambda^2} \right)^2 P(k_{b, \tau}) \int \frac{d\Omega d\nu}{X^2 Y} |A^*(\hat{s}, \nu) A(\hat{\Gamma}s, \nu)| |\phi(\nu)|^2 \\ & \quad \exp \left[-i2\pi\nu \left(\hat{s} \cdot \frac{b}{c} - \hat{\Gamma}s \cdot \frac{b'}{c} \right) \right]. \end{aligned} \quad (9)$$

So roughly speaking the cross multiplications of visibilities at a time delay in uv-space is proportional to the power spectrum times the Fourier transform of the cross multiplied beam pattern. We can then in principle combine information from different baseline pairs if we correct for the phase and normalization. As a check, when applied to equivalent baselines, $b = b'$, $\hat{s} = \hat{\Gamma}s$, and Eq.(9) reduces to Eq.(B9) of ?.

If this result is robust, then we can achieve all our goals stated in the introduction, i.e. to identify candidate baseline pairs, to find the optimal time offset, and to quantify the sensibility, by computing the integral in Eq.(9) for various time offsets. Thus we shall first test its robustness numerically.

3. ANALYSIS

3.1. Numerical Test

To test the robustness of Eq.(9), we need to compare the amplitude and phase of the integral for a pair of baselines with products of simulated visibilities of those baselines. For computational simplicity, we shall use a single frequency channel of 150MHz for the comparison. We may use this simplification without compromising generality because Eq. (9) is valid for a range of frequency channels if and only if it's valid for each single channels (i.e. when $\phi(\nu)$ is proportional to a delta function).

For the simulation, we take N random realizations of the sky on a healpix map (, ?) ¹. For each realization, each pixel is given a Gaussian random value of brightness temperature. We then rotate the baseline positions with the appropriate rotation matrix, recording the visibilities, for each baseline ². The resulting visibilities for the two baselines are then convolved via the Fourier convolution theorem, to obtain values of the cross correlation as a function of time-offset. The peak of the curve then corresponds to maximum redundancy. The accuracy of this result is limited by (simulated) cosmic variance and finite spacial resolution, and hence can be beat down by averaging over a large number of universes. A numerical estimate of the error of the peak height with $N = 1$ is $\lesssim 20\%$, and thus with $N = 2500$, we achieve an error of peak height $< 0.5\%$.

To test our understanding of the time-offset, and to

verify our derivation in Eq. (7), we must compare the simulated visibility cross multiplication with the integral in Eq. (7), for a pair of near-equivalent baselines. This comparison is show in Fig. 3.1. Since the sensitivity contribution is inferred from height of the peak of the cross-multiplied visibilities as a function of time. We first compare the simulation to the integral for a pair of equivalent baselines, then normalize the peaks of the near-equivalent baselines to that of the equivalent ones. In Fig. 3.1 we show on the top comparison of the convolution of an equivalent baseline of PAPER-128, normalized to 1 at the peak, whose location is at zero time offset as expected. On the bottom we show comparison of a near-equivalent baseline pair, of classes sep1,0:1,1 and sep1,1:1,1. The peaks are normalized with the same factor as the peak height on the top, i.e. the two plots have thus the same scale on the vertical axis. The height of the plot thus quantifies the added sensitivity. We see at a peak of around 0.055 sidereal days, or 1.32 hours, the two baselines are maximally redundant.

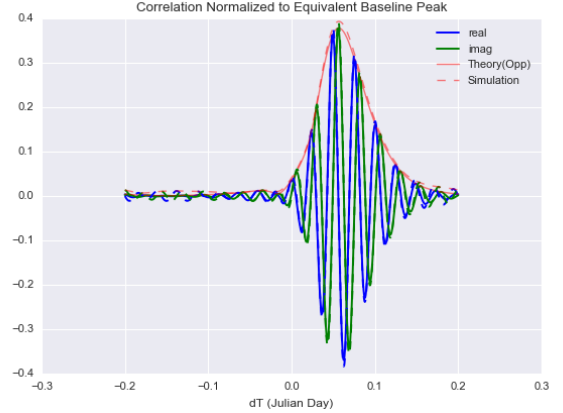


Figure 4. Numerical comparisons of the visibility correlation peaks to the Ω factor in Eq.(9). We generated 24000 instances of Gaussian random sky on healpix maps, computed visibilities and cross correlated them to find the correlation. We see that the theory and simulation line up in both amplitude and phase.

At the optimal time separation, the integral in Eq. (9) is maximized. Thus as another check we expect the two beams to have to same fringe pattern (frequency and phase). Due to the time delay, however, the beam center would be slightly shifted with respect to each other. This we show in Fig. 5. The left and middle panels show the beam fringe patterns for baselines sep2,0 and sep2,1, delayed by 0.0325 sidereal days, and the right panel shows their cross product. The fringe pattern indeed cancels out as we expect.

¹ We use functionalities in the python package AIPY for healpix mapping as well as coordinate transforms.

² As a caveat, there are two obvious ways to achieve the rotation. One can either fix the sky and rotate the baselines, or the

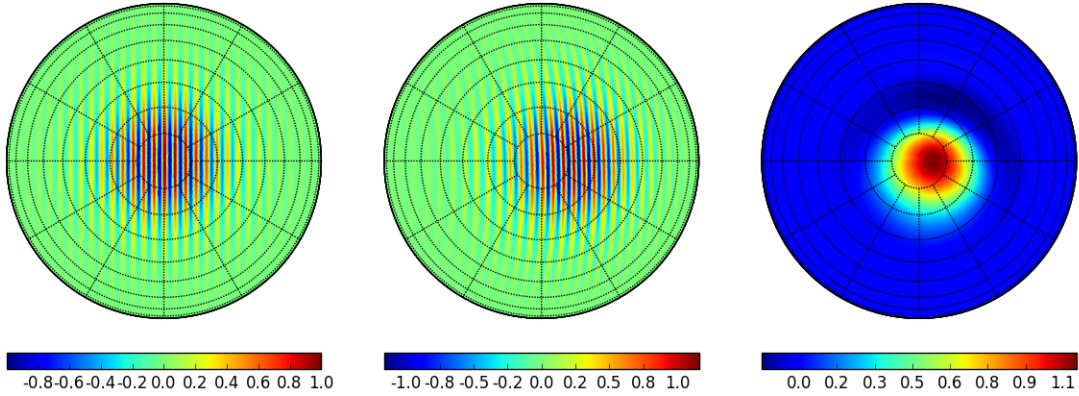


Figure 5. Beam fringe pattern of sep2,0(left), sep2,1 at a time delay (middle), and their conjugate product. Frequency of $\nu = 0.15\text{GHz}$ is chosen.

3.2. Expected Sensitivity Contributions

Having verified the validity of Eq.(9) from a single channel, we must point out that the peak height, or sensitivity contribution do depend on the frequency channels and shape of bandpass. This is because different frequency channels differ slightly in their phases at peak correlation and average incoherently. In Fig.?? we compare two channels 0.16 GHz and 0.17 GHz. Top panels shows the equivalent baseline pairs sep1,0 against itself, and bottom shows sep1,0 against sep1,1. We see that although the magnitude, drawn by the wide curves match up, the phases do not. This means the wider the frequency profile, the more destructive the interference, and lower the sensitivity contribution.

other way around. We found however, that we must not physically rotate the sky map, for the numerical round-offs due to finite resolutions of the map turns out to be significant. Thus we let the sky, represented by the healpix map, be fixed, and rotate the baselines.

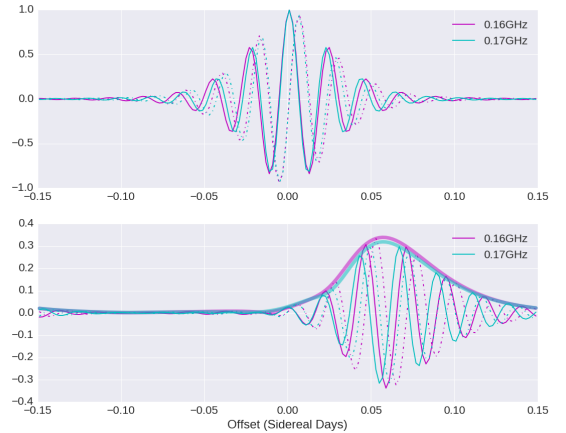


Figure 6. Comparisons of the peak phases of two different frequencies. Top panels shows equivalent baselines, bottom shows a pair of near-equivalents. The dot-dashed lines of each color are the imaginary parts, and the solid lines are the real parts. For near-equivalent case, we also draw the magnitude by the broad envelopes. We see that although the magnitude line up for two frequencies, the phases do not. This means there will be destructive interference when cross multiplying delay-space visibilities.

Having verified Eq. (7), we can thus predict the sensitivity contributions of a particular baseline pair simply by computing the integral. Intuitively we expect the sensitivity to depend on both the uv coverage of the baseline and the patch of sky inside the beam. A larger beam like PAPER-beam would tolerate larger time-offsets because more sky area can coincide in the two beams. To keep the flow of the discussion, we shall focus on results of PAPER-128, and present the results for HERA in the Appendix. Having computed all of the baseline pairs, we find that baseline pairs that are mirror images of each other give the same amount of redundancies (peak height), with the opposite time offset, as expected from symmetry. For example, sep1,0:1,1 is mirror image of sep1,0:1,-1 and these two baseline pairs give the same sensibility contribution. Thus in our results we shall only show a subset of representative baseline pairs that give different informations.

In the top panel of Fig. (3.2) below we show the peak heights and locations for a variety of baseline combinations. We see that baseline pairs that have crossings at a smaller time delay tend to have higher correlations. In other words, correlation peaks that are closer to zero time lag are higher. This is expected since a) the longer the time delay, the more the antennas have moved with respect to the sky and hence the less overlaps in patch of sky surveyed, b) smaller optimal time-offset corresponds to smaller differences in orientation, and hence in length of baselines in PAPER-64.

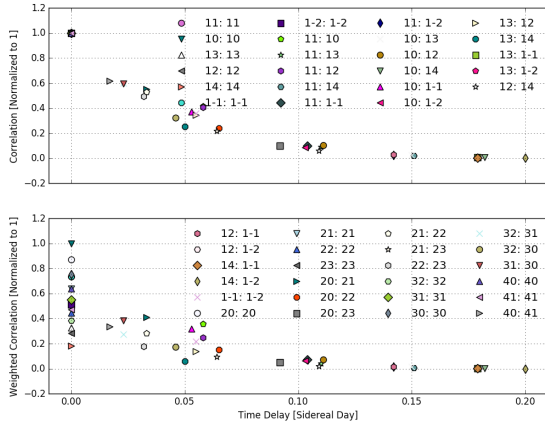


Figure 7. Relative sensitivity contributions of selected baseline combinations in PAPER-64. In the legend $m,n;p,q$ denotes cross multiplying PAPER-64 baselines of east-west, north-south separations (m,n) and (p,q) respectively. The top panel shows the peak height (degree of correlation) of each baseline combination, while the bottom panel multiplies the heights by the corresponding multiplicities as in Eq. (11), and in some cases an extra factor of 2 (explained in text). In weighting by the multiplicity (bottom), we have chosen to fix the sensitivity contribution of 1,0:1,0 to unity.

To determine that actual relative contribution to sensitivity of these baseline pairs, we have to take into ac-

count of the multiplicities of these baselines, or the size of the equivalency classes in a mathematical language. By these we mean how many physical antenna pairs have the same length and orientation. Looking at Fig. 3.2 we see for example sep1,0 will have higher redundancy than sep2,0, or sep1,1. The latest release of PAPER-64 data uses the 128-equivalent baselines sep2,1, sep2,0 and sep2,-1 ?, and achieved a 2σ upper limit of $22.4 mK^2$. There, the three sets of equivalent baselines are only cross multiplied by itself. Assuming that each baseline delivers the same quality of data (i.e. they have the same height of correlation peaks, which is in our normalization equal to unity), the relative contribution to sensitivity can be estimated.

First we can average of the visibilities of the baselines of the same separations. Since the core of PAPER-128 has 16 by 7 antenna configuration, there are $(16 - |m|) \times (7 - |n|)$ copies of the baseline $sepm,n$. This means that if we add visibility measurements of all these equivalent baselines, we get a factor of $\sqrt{(16 - |m|) \times (7 - |n|)}$ reduction in noise level. The sensitivity contribution of $sepm,n$, being the signal to noise ratio of the power spectrum, is thus proportional to $(16 - |m|) \times (7 - |n|)$. Next we can average over the power-spectrum taken from baselines of the different separations. Thus the total cumulative sensitivity is given by

$$\frac{P_S}{P_N} \propto \sqrt{\sum_{(n,m)} ((16 - |m|) \times (7 - |n|))^2}, \quad (10)$$

where the sum is only over pairs of m and n . If we now include power spectrum from cross-multiplications of near-equivalent baselines of types $sepm,n$ and $sepm',n'$, we get a general cumulative sensitivity:

$$\frac{P_S}{P_N} \propto \sqrt{\sum_{(n,m,n',m')} \Omega_{mn'm'n'} ((16 - |m|)(7 - |n|)(16 - |m'|)(7 - |n'|))}, \quad (11)$$

where Ω is the correlation peak height show in top panel of Fig. (3.2), and the sum is again only over tuples of m,n,m',n' . This form now includes the equivalent baselines in Eq. (10), with $\Omega_{m=m',n=n'} = 1$. Shown in the bottom panel of Fig. (3.2) is the peak heights weighted by this multiplicity factor (before taking the square root), with one difference. The difference is, since we have "folded over" the negative time delays, we have combined baseline pairs that are identical modulus parity, or in other words are mirror images of each other, by summing over them to get an extra factor of two. For example, instead of plotting 1,1:1,1 and 1,-1:1,-1 separately, we plot 1,1:1,1 with twice the multiplicity. Similarly, baseline pairs such as 1,0:1,1 also get the factor of 2 because they are identical to 1,0:1,-1. Baseline pairs such as 1,0:1,0, or 1,1:1,-1 do not get the factor of 2 because their mirror images are themselves.

3.3. Notes on Data, Foreground and Noise

Unlike the simulated clean EOR signal, real data are dominated by foreground and thermal noise, nei-

ther of which turns out to exhibit the correlation pattern seen in Fig. 3.1. Foreground exhibits long-range correlations and would lead to high responses at wide range of time-offsets. Instrumental noise for different baselines/antenna-pairs, on the other hand, are uncorrelated and thus exhibit responses consistent with zero at all time offsets. To illustrate, we use the second observing season of PAPER-128 data, taken from Jan. 21st to March 7th of 2014. To illustrate the effect of noise and foreground, we use the data before fringe-rate and

delay filtering.

4. CONCLUSION

APPENDIX

A. HERA ANALYSIS

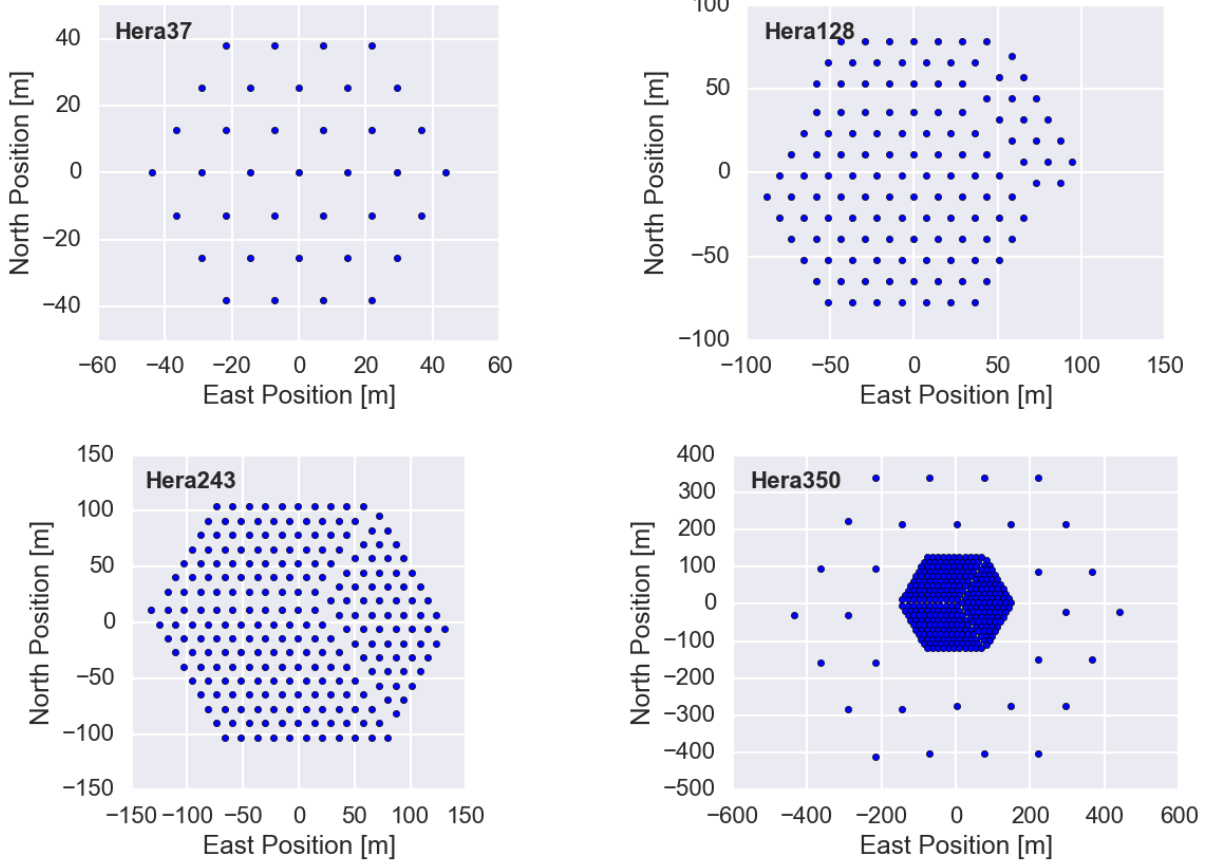


Figure A1. Planned Hydrogen Epoch of Reionization Array antenna configurations